Characterization and Modeling of UHF Wireless Channel in Terrestrial SFN Environments: Urban Fading Profiles

Sungjun Ahn, *Member, IEEE*, Jeongchang Kim, *Senior Member, IEEE*, Seok-Ki Ahn, *Member, IEEE*, Sunhyoung Kwon, *Member, IEEE*, Sungho Jeon, *Senior Member, IEEE*, David Gomez-Barquero, *Senior Member, IEEE*, Pablo Angueira, *Senior Member, IEEE*, Dazhi He, *Member, IEEE*, Cristiano Akamine, *Member, IEEE*, Mats Ek, Sesh Simha, Mark Aitken, *Member, IEEE*, Zhihong Hunter Hong, Yiyan Wu, *Fellow, IEEE*, and Sung-Ik Park, *Fellow, IEEE*

***Abstract*—This paper proposes several realistic fading channel models to describe the signal distortions that arise in single frequency network (SFN) environments. The proposed models characterize ultra-high frequency (UHF) wireless channels based on measurements from operating networks in metropolitan areas. In this paper, the unique features of SFN transmission are identified compared to the conventional, single antenna transmission channels. The impacts of urban propagation, tower configuration, and mobile and terrain effects are considered based on the tapped delay line structure. The proposed models can provide a useful reference to facilitate the SFN system design, network planning, verification, and receiver performance test. Free MATLAB source code of the fading simulator is available at https://github.com/ETRI-KMOU/FadingChannelSimulator.**

***Index Terms* — Single frequency network (SFN), channel modeling, ultra-high frequency (UHF) radio propagation.**

This work was supported by Institute of Information & Communications Technology Planning & Evaluation (IITP) grant funded by the Korea government (MSIT) (2020-0-00846, Development of Convergence Transmission and Technology for 5G and ATSC 3.0 Networks) *(Corresponding author: Sung-Ik Park).*

Sungjun Ahn, Seok-Ki Ahn, Sunhyoung Kwon, and Sung-Ik Park are with the Media Research Division, Electronics and Telecommunications Research Institute (ETRI), 218 Gajeong-ro, Yuseong-gu, Daejeon, 305-700 South Korea (e-mail: {sjahn, seokki.ahn, shkwon, psi76}@etri.re.kr)

Jeongchang Kim is with the Interdisciplinary Major of Maritime AI Convergence, the Division of Electronics and Electrical Information Engineering, Korea Maritime and Ocean University (KMOU), Busan, 49112, South Korea (e-mail: jchkim@kmou.ac.kr)

Sungho Jeon is with Media Transmission Department, Korean Broadcasting System, Seoul 07235, South Korea (e-mail: jeonsh@kbs.co.kr).

David Gomez-Barquero is with the Institute of Telecommunications and Multimedia Applications, Universitat Politecnica de Valencia, 46022 Valencia, Spain (e-mail: dagobar@iteam.upv.es).

Pablo Angueira is with the Department of Communications Engineering, University of the Basque County, 48013 Bilbao, Spain (e-mail: Pablo.angueira@ehu.eus)

Dazhi He is with the School of Electronic Engineering, Shanghai Jiao Tong University Shang Hai 200240, China (e-mail: hedazhi@sjtu.edu.cn)

Cristiano Akamine is with the School of Engineering, Mackenzie Presbyterian University, Sao Paulo, SP Brazil (e-mail: cristiano.akamine@mackenzie.br).

Mats Ek is with Progira Radio Communication, AB, Luleå 97775, Sweden (e-mail: mats.ek@progira.com)

Sesh Simha and Mark Aitken are with ONE Media 3.0, Sinclair Broadcast Group, Inc., Hunt Valley, MD 21030 USA (e-mail: {ssimha, maitken}@sbgtv.com)

Zhihong Hunter Hong and Yiyan Wu are with Communications Research Centre Canada, Ottawa, ON, K2H 8S2, Canada (e-mail: zhihonghunter.hong@ised-isde.gc.ca, yiyan.wu@ieee.org).

This work was partially presented at IEEE BMSB in 2022 [87].

I. Introduction

RECENTLY, the art of contemporary broadcasting has successfully migrated into single frequency networks (SFNs) [1]-[6]. SFNs were first planned in Europe in the early 2000s and have been widely deployed in most European countries using the first-generation standard DVB-T [7], [8]. Lasted the efforts for a decade, the SFN allotment has finally been embodied in other ITU-R regions. Seeking the spectrum economy in use, the latest specifications of terrestrial broadcast systems, e.g., Advanced Television Systems Committee (ATSC) 3.0 and Digital Video Broadcasting-2nd Generation Terrestrial (DVB-T2), have been designed to be SFN-based or at least SFN-friendly [9], [10]. Notably, province-scale SFNs in South Korea and the United States have already commenced public services of ATSC 3.0 to cover numbers of cities and are foreseen to expand nationwide.

Although primarily devised to resolve the spectrum scarcity challenge, SFNs feature advantages such as macro-diversity and flexible coverage improvement using gap-fillers [11]-[13]. SFNs present more homogeneous coverage percentages over the service area compared to multiple frequency networks (MFNs). This lower signal variability distribution benefits mobile and portable reception. At the same time, the spotlight on in-vehicle entertainment has also reinforced the role of SFN for mobile entertainment services [14]-[17]. The SFN advantages further allow the broadcasters to imagine highly flexible network compositions such as cloud transmission and local service insertion [18], [19].

The use of SFN has not only been limited to broadcasters but has also been a matter of interest to the general wireless industry [20], [21]. The cellular communication sector has introduced SFN features into its multicast mode architecture, namely, multimedia broadcast/multicast service (MBMS) [22]-[26]. Such a concept known as multicast-broadcast SFN (MBSFN) has been adopted in the 3rd Generation Partnership Project (3GPP) standards since Rel-7 [27], [28]. The 3GPP MBSFNs have long sought a low-power low-tower (LPLT)-based architecture for the sake of compatibility with legacy cells, but lately, the enablers are envisaging an integration of high towers as well to meet emerging

requirements. To this end, the recent progress in Rel-16 has strengthened the MBSFN capability by introducing new numerologies with a longer-length cyclic prefix (CP) and better mobility tolerance [29]-[32].

Nevertheless, the community still lacks a convincing model describing the channel characteristics of SFNs in the wild. Despite the previous efforts, even seldomly made [8], the existing models have less reflected the physical properties of genuine, state-of-the-art SFNs deployed in practice. The absence of a reliable reference channel profile may misguide the system design and network planning to lay significant inefficiency. This paper addresses this problem and proposes several fading channel models by extracting the realistic features of modern SFNs, in terms of delay spread, Doppler behavior, tap attenuation, and other relevant parameters. The models incorporate channel impulse response (CIR) profiles designed to match measurements taken in commercial SFNs. The modeling in this paper targets the ultra-high frequency (UHF) band environment. Results are proposed for networks operating in frequencies within the 400 ~ 800 MHz range.

Table I is an overview listing the models proposed in this paper [1]. Note that this paper principally looks into urban scenarios. Focusing on metropolis service areas, high-power high-tower (HPHT) and LPLT networks are investigated in parallel [33], [34]. CIR attributes are hence defined independently for HPHT and LPLT, considering their intrinsic differences. The models are built based on empirical data gathered on actual network deployments. Specifically, the channel models proposed for HPHT SFNs are based on precise measurements taken in an on-air network's service area in the Seoul Metropolitan area, South Korea. The LPLT SFN models are designed following a commercial network deployment in Bengaluru, India. The LPLT channel profiling leverage computer simulations with geographic information and network system data from the Bengaluru case. Pointing out that SFNs could be formulated as a mixture of high and low towers, an empirical model for mixed SFN is also presented.

The proposed SFN channels are designed for the orthogonal frequency division multiplexing (OFDM) systems. The nature of the model is microscopically explored by identifying how the SFN physical environment impacts the OFDM signals. Accordingly, the results will be applicable to general variants of SFNs, such as coordinated multipoint (CoMP) and distributed antenna systems [35], [36].

The remainder of this paper is organized as follows. Section II describes the motivation of this work. Section III describes the field-measured CIRs and the modeled SFN channel profile of the HPHT network first. Section IV, in parallel, introduces the simulations and analysis of SFN channel models for LPLT environments. Section V presents the model for mixed SFN configuration having both high and low towers integrated, and Section VI discusses the future applicability and other related miscellanies. Section VII concludes the paper with a summary.

[1] As part of this project, a channel simulator software is developed and released (S_3, S_2, S_1, *India-U*, and *India-R* are available). Free MATLAB source code is available at https://github.com/ETRI-KMOU/FadingChannelSimulator.

TABLE I. BRIEF DESCRIPTIONS FOR PROPOSED CHANNEL MODELS

Notation	Location	Description
S_3 Fixed	Seoul Metropolitan, South Korea (HPHT)	Three LoS and three NLoS components, stationary channel scenario
S_3 Mobile		Three LoS and three NLoS components, mobile reception scenario
S_3-Extended (Fixed/ Mobile)		Extension of S_3: Three LoS and six NLoS components (including additional multipaths from the original model), extensions for stationary and mobile models, respectively
S_2 Fixed		Two LoS and three NLoS components, stationary channel scenario
S_2 Mobile		Two LoS and three NLoS components, mobile reception scenario
S_1 Fixed		Single LoS and five NLoS components, stationary channel scenario
S_1 Mobile		Single LoS and five NLoS components, mobile reception scenario
India-U	Bengaluru, India (LPLT)	Twenty NLoS components
India-R		Four LoS and fourteen NLoS components
J_2 Fixed	Jeju Island (Suburban), South Korea (Mixed)	Two LoS and two NLoS components, stationary channel scenario
J_2 Mobile		Two LoS and two NLoS components, mobile reception scenario

II. MOTIVATION AND PRELIMINARIES

A. Background and Motivation

Unlike the traditional single transmitter case, SFN field studies require complex infrastructure and methodologies, specially if the application scenario is a large urban environment. The efforts portraying realistic SFN channel models have hence been found scarce so far. However, SFNs deserve particular investigation as they present distinctive identities. SFN channels endow with unique properties that stem from the multi-source topology of SFNs: (*i*) a large delay spread which attributes notably preceding and lagging arrivals; (*ii*) plural line-of-sight (LoS) connectivity; and (*iii*) unstructured fluctuations over the power-delay profile.

The most tangible point is the wide delay spread, which exceeds that of the single-cell instances manyfold. This feature comes from the fact that the user in SFN can detect both signals from far-distant transmitters and in-proxy transmitters. Such an aspect is intimately bound with another property, the unstructured power-delay profile. SFN power-delay profiles present ambiguous location and fading features that vary with the network deployment structure. On the contrary, the single-cell scenario is simplified because the multipath becomes significantly attenuated by reflection and diffraction. Their power-delay profiles decay monotonically, allowing the lagging components to be negligible in most cases.

Most standard fading channel models have assumed that a single transmitter is responsible for every signal arrival. Multipath echoes have been the only concern for description, and hence the CIR taps therein have not lagged more than 15 μs. Table I summarizes this aspect by listing the hindmost delays of normative channel models. Note that most models confine energy within 10 μs. For example, the popular mobile TU-6 and stationary RC20 channels have maximum delay spreads of 0.5 μs and 5.4 μs, respectively [37]-[39]. Brazil-B, HT-20, and ITU-Vehicular B examples describe 12.7 μs ~ 20 μs lagging

TABLE II. LIST OF THE DELAY AND RELATIVE GAIN OF THE HINDMOST ECHO IN EXISTING CHANNEL MODELS [16], [37]-[42], [45], [46]

Channel Model	Hindmost Delay [us]	Path Gain [dB]
Rural Area (RA)-6 (COST 259)	0.5	-22.4
Typical Urban (TU)-6 (COST 207)	5.0	-10.0
Typical Urban (TU)-20 (COST 259)	2.14	-24.3
Hilly Terrain (HT)-20 (COST 259)	18.0	-30.7
RC20 (P1, DVB)	5.4	-17.9
RL20 (F1, DVB)	5.4	-7.8
0 dB Echo (DVB)	0.9×GI	0.0
ITU-Vehicular B	20.00	-16.0
Portable Outdoor (PO)	5.7	-19.3
Portable Indoor (PI)	9.2	-11.2
Brazil-A	5.93	-16.4
Brazil-B	12.70	-22
Brazil-D	5.93	-2.8
Brazil-E	2.00	0.0
SARFT-8	31.80	0.0
Modified TU-12 in [16]	45.0	-15.0

components, but those components are instead defined with significant attenuation with respect to the main path [40]-[44].

In fact, studies in real SFNs have reported delays greater than 30 μs, even exceeding 73 μs under certain conditions [45]. ATSC 3.0 has already foreseen that SFNs would face such issues and defined up to 703.70 μs length of guard intervals (e.g., CP) so that the system could be immune to 211 km difference of propagation distances [1]. Saving the overhead cost, the operating ATSC 3.0 systems may prefer guard intervals in a range of 148.15 μs ~ 296.30 μs (i.e., 44 km ~ 88 km propagation difference).

The primitive SFN-oriented channel model SARFT-8 has previously addressed a large delay spread, where its hindmost delay reaches 32 μs [46]. However, this previous model focuses only on the strong echoes and overlooks the possibility of moderate echoes. The side-echoes are defined to be 20 dB lower than the main path. This aspect makes SARFT-8 channel often viewed as an SFN with only two towers accompanying negligible multipath. The Brazil-E channel considers another interesting case with three 0 dB echo components within 2 μs. The modified TU-12 model in [16], is just a repetition of the TU-6 channel having the replica be 40 μs delayed and 5 dB attenuated from the original TU-6 tap cluster.

These legacy SFN models are too specific, whereas SFNs in the wild show multiple contributions from many transmitters with different emission properties. Moreover, the existing SFN channel models lack a careful design for dynamic Doppler perturbation. In fact, such undercharacterization can trigger a crucial degradation in (dependently) optimized OFDM systems; where delay spread, Doppler perturbations, and the shape of CIR contribute to the performance. These consequences necessitate an accurate model to encourage efficient deployment, signal optimization, and design of high-performance devices.

Based on the tapped delay line (TDL) model, this work introduces strong echoes with large delays into the SFN channel model, along with pre-ghosts. Simultaneously, the model includes complex Doppler behaviors to describe SFN's composite LoS/non-LoS (NLoS) contributions [47]. The proposed models rely majorly on the empirical measurements obtained from ATSC 3.0 networks. Note that the ATSC 3.0 physical layer is based on coded OFDM and quadrature amplitude modulation (QAM) schemes. Thus, the presented results will be suitable for most wireless systems operating in similar frequency bands [1], [48].

B. HPHT SFN vs. LPLT SFN

HPHTs, as a contrastive terminology against LPLTs, typically designate the transmitters elevated at least 150 m above the earth where the target users are at [34]. The height of HPHTs reaches 300 m in general, and the effective radiated power (ERP) reaches tens of kilowatts. On the contrary, LPLT transmitter antennas are located at heights below 40 m (above the service area). In generic understandings, LPLTs target way smaller service areas than HPHTs, and their ERPs do not lie in a kW scale.

Compared to HPHT, LPLT SFNs show denser site distributions if similar coverage percentages are sought. Accordingly, urban LPLT SFNs will present more complex CIRs. Instead, the low-powered emission property allows neglecting the contributions from distant transmitters, unlike the HPHT case.

C. Basics for Measurements – Transmitter Identification and Channel-Sounding

This work, particularly the works in Section III and V, exploits the channel-sounding data recorded in a commercial SFN[2]. The measurements are taken over the radio channel conveying on-air services. To this end, the experiments use a digital television (DTV)-native channel-sounding technology referred to as transmitter identification (TxID) [49]-[51].

TxID is a watermarking tool identifying each SFN transmitter's signals from the mixture of them, so their contribution to the overall energy distribution can be accurately quantified. TxID itself involves channel-sounding and radiographs the signal responses by leveraging sequence correlation properties [52]. That is, the receiver cross-correlates the received signals with reference TxID sequences to measure the excited channel's multipath profile. In ATSC 3.0 systems, TxID utilizes the direct sequence spread spectrum (DSSS) with binary-modulated Gold code sequences of size 8192 [1], [53].

The 8192-length TxID sequences provide a processing gain of 39.1334 dB. On the other hand, a cross-correlation between different ATSC 3.0 TxID sequences can return three possible outcomes: -1, -129, and 127 [49]. In turn, approximately 19 dB headroom is guaranteed for the auto-correlation peak over the cross-correlation *floor*. On this account, the experiments in this paper consider the channel-sounding results to have at most 19 dB resolution.

In our experiments, the TxID signals are generated with 6.912 MHz baseband sample rate, offering a precision of 144.67 ns for each channel-sounding. Sequence correlations are applied over the baseband samples obtained at a 6.912 MHz

[2] LPLT channel modeling in Section IV relies on geographic data-based simulations (see Section IV for detailed procedures).

sampling rate. As for the measurement system, the CIR capturing submodule is driven by a 14-bit analog-to-digital converter (ADC). Raw radio signals are first oversampled in 55 MHz rate; down-sampled into 20 MHz sampling rate for intermediate frequency (IF) operations in subsequence; and finally distilled into the baseband elements that will be used for extracting the power-delay profiles. The cross- and auto-correlations are executed over a 2048 sample-sized window, hence allowing ±148.15 μs observations around the main signal tap. Without loss of generality, the demodulator clock is tuned at the strongest incidence chosen as the main tap. In addition, the noise is minimized across the measurements by ensemble averaging, preamble cancellation [50]-[51], or Hilbert-Huang transform [54]. As a result, every correlation peak is distinguishable down to –19 dB from the strongest component.

III. Field-Measured Profile and Channel Modeling in High-Power High-Tower Environment

This section first introduces several channel response models that render the UHF channel characteristics in HPHT SFNs. The presented models are empirically built on the measurement results, which were obtained from an operating network in the Seoul Metropolitan area, South Korea. We incorporate various possibilities of reception instances, in which the classes of channel profiles are accordingly defined as outlined in Table I. Each model class characterizes distinct signal response configurations, particularly by varying the number of LoS components and including/excluding the mobility effect. Every channel element is carefully defined to replicate the radio reception environment observed in the field.

A. HPHT SFN Network Infrastructure in Seoul (South Korea) and Field Observations

South Korea launched SFN-based DTV services in 2017, being the first starter for ATSC 3.0 [55]. Currently, the SFNs are deployed on a metropolitan scale[3], followed by a plan to expand the SFN nationwide. The SFN of Seoul Metropolitan is currently the largest and densest DTV SFN in South Korea and consists of ten synchronized transmitters with static inter-tower delays [56].

The experiments utilized the 701 MHz (CH 52) and 768 MHz (CH 56) UHF channels conveying ultra-high-definition DTV services. Over a single radio bandwidth, a coordinated service area has been created across the SFN transmitter's coverages as enabled by studio scheduling. Each transmitter has been controlled through dedicated fiber, satellite, or microwave links based on the A/324 studio-to-transmitter link (STL) protocol [57]. Note that the SFN transmissions may not be *strictly synchronous*: Transmitters are allowed to emit the same frame at different times from each other to shape the network coverage desirably. This aspect complicates predicting the power-delay profile further beyond. As for ATSC 3.0, dedicated signaling bits are defined in STL transport protocol to notify the offsets from the pivot emission time [57], [29].

[3] Five metropolitan SFNs have been deployed at the first stage in 2017.

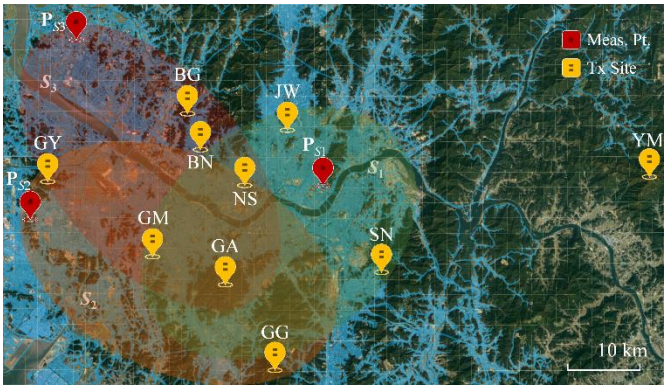

Fig. 1. Geographic topology of the Seoul Metropolitan SFN.

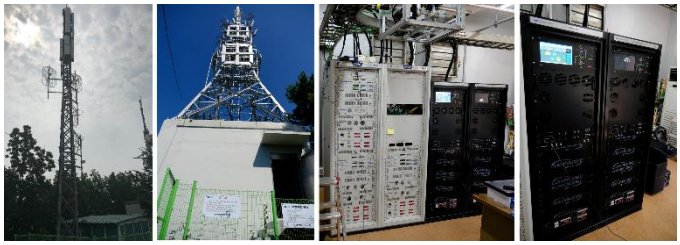

Fig. 2. Transmitter facilities of the Seoul Metropolitan SFN.

TABLE III. SFN Towers in The Seoul Metropolitan Area

Site Indicator	HPA Power	Vertical Datum [m]	Antenna Height [m]	Antenna Gain [dBi]	Antenna Config.	ERP [kW]
NS	5 kW	243	109	7.79	2:2:2:2	19.2
GA	5 kW	620	49	10.81	4:4:4:4	39.6
GG	2 kW	514	86	7.79	2:2:2:2	7.96
GY	2 kW	380	70	7.79	2:2:2:2	8.11
YM	2 kW	1,139	28	10.81	4:4:4:4	17.5
BG	900 W	231	28	7.79	2:2:2:2	4.01
BN	900 W	210	28	7.79	2:2:2:2	4.01
JW	900 W	154	28	7.79	2:2:2:2	4.23
SN	900 W	407	24	10.82	1:1:0:0	30.2
GM	900 W	150	19	4.77	2:2:2:2	29.8

Fig. 1 shows the tower deployment in the Seoul Metropolitan area [58]. Ten transmitters, located in elevated sites, were part of the SFN where the measurements were conducted. Table III gathers the elevation data of each tower's position. For instance, site GA[4] is 615 m above sea level and the tower has an additional height of 50 m. Such arrangement fits in the definition of HPHT since populated residential areas in Seoul Metropolitan, in contrast, are typically located at 15 m ~ 60 m above sea level [59].

The Seoul SFN consisted of pure STL-connected transmitters only, without including any repeaters. Every transmitter could then inject unique TxID signals, which were leveraged for channel-sounding. An equal injection level of -9.0 dB was applied for every transmitter's TxID signal, thereby allowing a fair gauging of each transmitter's contribution. That is, the TxID signals had 9 dB lower power than the broadcast service signals.

The ERP level of each tower ranged from several kilowatts

[4] The towers' labels are named after the abbreviation of each site location.

to tens of kilowatts, making up a multi-class network topology[5] as specified in Table III. In terms of high-power amplifier (HPA) output, three classes of transmission have been considered: 5 kW, 2 kW, and 900 W. The largest transmitter was GA with 50 kW ERP. Overall achieving 10.81 dBi gain thereat, arrays of panel antennas were mounted in a 4:4:4:4 formation, i.e., each for four layers in a column, where the panels were installed to head onto perpendicular directions to each other (0˚, 90˚, 180˚, and 270˚). Fig. 2 illustrates some of the infrastructures in sites SN and GM, representative of typical HPHT transmission systems.

1) Field Measurement Procedures and Obtained Data

The measurements took place on plain land or low-rise terrains in three different environments. The models S_3, S_2, and S_1 concern locations $\mathbf{P}_{S3}$, $\mathbf{P}_{S2}$, and $\mathbf{P}_{S1}$ where the receiver experienced LoS propagation links with three, two, and one transmitter of the SFN network, respectively. In order to seize a versatile usage applicable to both stationary and mobile scenarios, the locations were selected to be close to (or exactly on) roadways present in those spots [60]. The altitudes of $\mathbf{P}_{S3}$, $\mathbf{P}_{S2}$, and $\mathbf{P}_{S1}$ were 20 m, 50 m, and 70 m above sea level, respectively.

The field data were collected at a mobile facility integrating a set of professional measurement equipment. A vehicle-type facility was custom-built to include an advanced ATSC 3.0 demodulator with TxID-aided CIR tracking functionality, a spectrum analyzer, a Global Positioning System (GPS) tracker, and an antenna feed monitor. The CIR observations were recorded by being coupled with GPS logs and coordinated map data [61]. The UHF antenna was mounted on a mast to facilitate measurements at variable heights within the range from 1.9 m to 9 m. Precisely, an omnidirectional antenna with a gain of 0 dBi was used. To be clarified, the GPS and UHF antennas were aligned with the center spine of the vehicle. The antennas were isolated from undesired mutual coupling by securing more than a single wavelength ($\simeq$ 0.43 m for 700 MHz) spacing from each other, but not much distanced to violate the validity of location information.

The practical rationale was built behind the modeling through experiments. The field experiments were comprehensively conducted along with heuristic inspections for geographic environments. To summarize, the LoS paths from GY, BG, and GA towers were visible at $\mathbf{P}_{S3}$; while $\mathbf{P}_{S2}$ could capture the LoS links from GA and GY; and that of GA was available at $\mathbf{P}_{S1}$.

Fig. 4 illustrates one of the channel-sounding results, the data measured at $\mathbf{P}_{S3}$ for S_3 scenario modeling. The impulse response included all the ingredients of the HPHT SFN channel model under study. On the one hand, there were a group of six spectral lines coming from six different transmitters, i.e., GY, GA, BG, BN, NS, and GM, including significant pre-ghosts and long-delayed echoes. The shadowing effect was also exhibited, as the signal from JW was not received while being closer than other SFN transmitters (see Fig. 1). Moreover, it was shown as

[5] Depending on the regulations of each country, the grant for radiation power is often classified into multiple tiers.

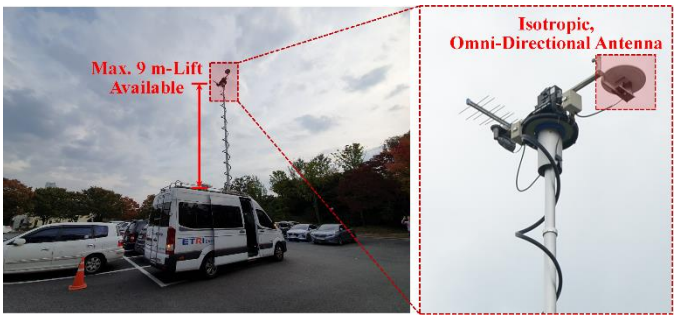

Fig. 3. Test vehicle and measurement antennas.

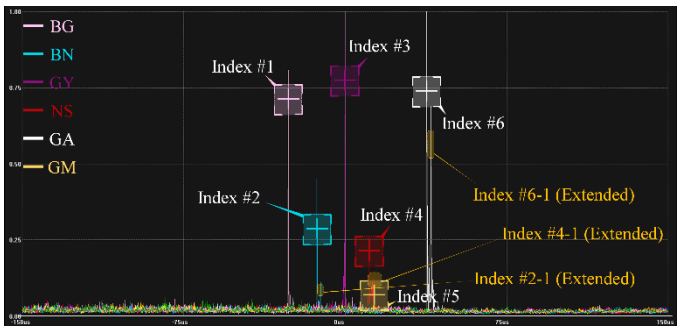

Fig. 4. SFN channel profile measured at $\mathbf{P}_{S3}$, Seoul Metropolitan (S_3 scenario, centered at 701 MHz, 6 MHz-width ATSC 3.0 DTV channel).

well that CIRs in SFN topology are likely to pose considerable multipath distortions because the power-delay profile did not decay monotonically by delay.

On the other hand, the NLoS incidences from BN, NS, and GM were found quite comparable to the LoS counterparts. This result again encourages designing new SFN channel models because the precedent models have modeled the NLoS contributions negligibly. Based on the empirical rationale obtained, the proposed channel models are expected to describe well the complicated channel behavior in urban SFNs, which could not be replicated by existing models. The measurement results are refined into the models described in Table IV-VII.

B. Channel Modeling: 3-LoS Case (S_3) – Stationary Environment

For reduced complexity in simulations, the TDL models in S_3 are limited to six different CIR taps. Derived from Fig. 4, *S_3 Fixed* and *S_3 Mobile* models each consist of three LoS taps (stand for GY, GA, and BG) and three NLoS taps (correspond to BN, NS, and GM). To this end, a single strongest CIR peak is extracted from the multipath profile of each accessible tower. Every CIR tap is considered to be resolvable from each other, as a set of non-resolvable components can be seen as a single CIR tap [62]. In other words, each tap in S_3 models belongs to a different, distinguishable bin in the time domain so that the phase distortion (i.e., fading effect) is considered individually for each tap [63]. The resultant formulations of S_3 models follow below.

Let us define Ω_L and Ω_N to be the indicator sets of LoS and NLoS taps, respectively. Following the configuration in Table IV, one can write $\Omega_L = \{1, 3, 6\}$ and $\Omega_N = \{2, 4, 5\}$ for S_3, and the time-domain impulse response of *S_3 Fixed* channel can be expressed as

TABLE IV. HPHT SFN CHANNEL MODEL PROFILE: S_3 *FIXED*

Tap Index	Rel. Power [dB]	Rel. Delay [us]	Type	Phase Shift [rad]
1	-0.96	-26.041666667	LoS	5.235988
2	-3.65	-12.876157407	NLoS	4.855121
3	0.00	0.000000000	LoS	0.000000
4	-6.03	10.995370370	NLoS	3.419109
5	-13.74	13.165509259	NLoS	5.864470
6	-0.17	37.471064814	LoS	4.683297

TABLE V. HPHT SFN CHANNEL MODEL PROFILE: S_3 *MOBILE*

Tap Index	Rel. Power [dB]	Rel. Delay [us]	Type	Doppler Spectrum
1	-0.96	-26.041666667	LoS	Pure Doppler (0.7771f_d shift)
2	-3.65	-12.876157407	NLoS	Classical
3	0.00	0.000000000	LoS	Pure Doppler (-0.3160f_d shift)
4	-6.03	10.995370370	NLoS	Classical
5	-13.74	13.165509259	NLoS	Classical
6	-0.17	37.471064815	LoS	Pure Doppler (0.4312f_d shift)

TABLE VI. HPHT SFN CHANNEL MODEL PROFILE (EXTENDED VERSION): S_3-*EXTENDED*

Tap Index	Rel. Power [dB]	Rel. Delay [us]	Type	Phase Shift [rad] (Stationary)	Doppler Spectrum (Mobile)
1	-0.96	-26.041666667	LoS	5.235988	0.7771f_d shift
2	-3.65	-12.876157407	NLoS	4.855121	Classical
2-1	-9.41	-11.140046296	NLoS	2.215894	Classical
3	0.00	0.000000000	LoS	0.000000	-0.3160f_d shift
4	-6.03	10.995370370	NLoS	3.419109	Classical
4-1	-8.17	13.454861111	NLoS	3.758058	Classical
5	-13.74	13.165509259	NLoS	5.864470	Classical
6	-0.17	37.471064815	LoS	4.683297	0.4312f_d shift
6-1	-1.27	39.496527778	NLoS	5.430202	Classical

$$h_{\mathrm{F}}(t)=\sum_{i\in\Omega_{\mathrm{L}}}\sqrt{\rho_i}e^{-j\theta_i}\delta(t-\tau_i)+\sum_{k\in\Omega_{\mathrm{N}}}\sqrt{\rho_k}e^{-j\theta_k}\delta(t-\tau_k) \quad (1)$$

for an arbitrary time instant $t \in \mathbb{R}$, where $\rho_i \in (0, 1]$, $\tau_i \in \mathbb{R}$, and $\theta_i \in [0, 2\pi)$ denote the normalized magnitude[6], relative arrival delay, and relative phase shift of the i ($\in \Omega_{\mathrm{L}}$ or Ω_{N})th tap, respectively; and $\delta(\cdot)$ implies the Dirac-Delta function. Every attribute of each tap (i.e., gain, delay, and phase shift) is defined relative to the main path, Tap #3. Being S_3 *Fixed* channel a stationary channel, every attribute of this model is defined to be time-invariant. The phase shifts are then considered fixed as well. Note that the LoS and NLoS components originate from physically different layouts, which will result in different phase statistics.

The phases of LoS taps are calculated directly from the measured delay profile. The phase shift $\theta_{i\in\Omega_{\mathrm{L}}}$ of LoS tap #i is given by $\theta_i = 2\pi\ \mathrm{rem}(f_c\tau_i)$, where $f_c > 0$ denotes the center frequency; rem(x) denotes the residue function $\mathrm{rem}(x) \triangleq \mathbf{1}(x < 0) + |x| - \lfloor |x| \rfloor$ with respect to $^{\forall}x \in \mathbb{R}$; and $\mathbf{1}(\cdot)$ denotes the Boolean indicator function. Throughout this section, we use f_c = 700 MHz as a representative figure of UHF channel and derive every phase shift value on 700 MHz frequency.

[6] The normalization is applied to make the aggregate channel power $\sum_{i\in\Omega_{\mathrm{L}},\Omega_{\mathrm{N}}}\rho_i$ equal to 1. For the case of Table IV, the normalized magnitude of Tap #1 ρ_1 = 0.2299 (= −6.3839 dB) is given by dividing $10^{-0.96/10}$ by the net sum of relative power of every tap.

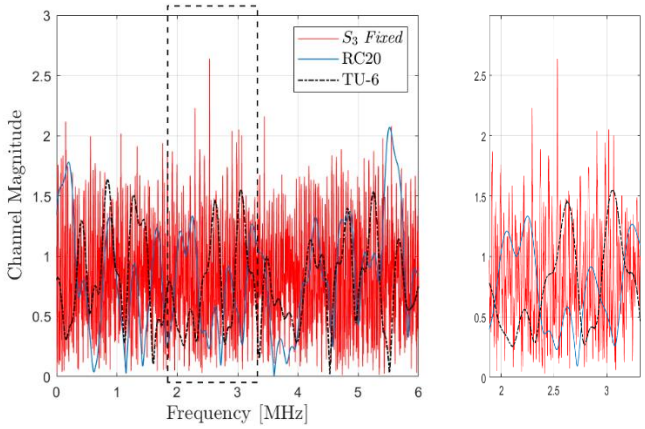

Fig. 5. Frequency response of S_3 *Fixed* channel.

It is considered a better approach to use delay measurements for deriving phase shifts, compared to using geographic distance information. This delay-based definition can incorporate the effect of intentional timing offsets across the transmitter emissions, where modern SFNs can deliberately *shape* the network by assigning different emission times to the transmitters [1], [29], [48], [57].

The phase shifts in NLoS taps can be considered random samples [64]. For coherence with previous models, the phase shift values Ω_N are sampled from RC20 (DVB-F1) and RL20 (DVB-P1) models suggested by DVB.

Due to the substantial contributions of effective multipaths, S_3 *Fixed* channel shows quite severe frequency selectivity. For comparison purposes with precedent channel models, Fig. 5 illustrates the simulated frequency response of S_3 *Fixed* channel over a 6 MHz radio bandwidth. S_3 *Fixed* is found to exhibit heavier fluctuations than RC20 and TU-6 models [37]. Therefore, demodulators would need more delicate channel estimation and interpolations to operate in urban SFNs.

C. Channel Modeling: 3-LoS Case (S_3) – Mobile Reception Environment

A Doppler model is incorporated to S_3 *Mobile* described in Table V. This model includes three LoS components, whereas the rest of the taps are NLoS energy contributions. Notably, the Doppler components are modeled to identify statistical differences between the LoS and NLoS components. For LoS signals, the proposed model assigns a pure Doppler shift to the CIR tap #$i \in \Omega_L$ as

$$f_{s,i} = \alpha_i f_d, \quad (2)$$

where $f_d = vf_c/c$ denotes the maximum Doppler shift dependent on the user speed $v > 0$ and the speed of light $c \simeq 3\times10^8$ m/s. The relative scaling coefficients are herein defined as α_1 = 0.7771, $\alpha_3 = -0.3160$, and $\alpha_6 = 0.4312$ [7].

Note that the amount of Doppler shift depends on the

[7] $\alpha_1 = \cos(39°)$, $\alpha_3 = \cos(64.4584°)$, $\alpha_6 = \cos(108.4215°)$ (see Fig. 6).

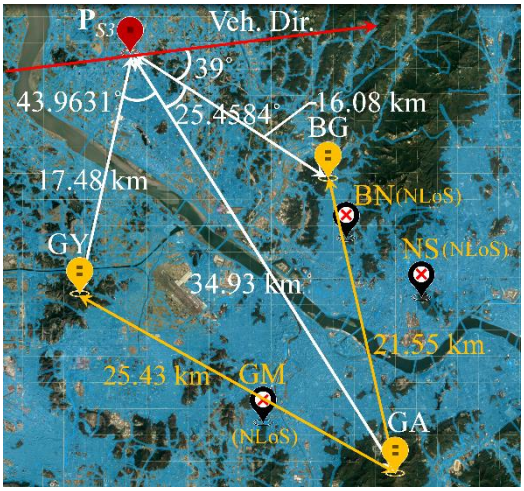

Fig. 6. Description of S_3 *Mobile* situation.

terminal's relative velocity projected onto the source direction. In this regard, the Doppler-scaling coefficients are carefully derived from the actual GPS coordinate records. Geometrically, the transmission sites BG, GA, and GY[8] are 16.08, 34.93, and 17.48 km, respectively, distant from the measurement point $\mathbf{P}_{S3}$ located at (37°42'26.52"N, 126°45'19.15"E). The segments BG-GA and GA-GY, in addition, span 21.55 and 25.43 km, respectively. The properties of triangles then give the contained angles at the vertex $\mathbf{P}_{S3}$. In turn, angular positions of the sources BG, GA, and GY are computed relative to the vehicle's heading direction, i.e., the estimates of $\cos^{-1}(\alpha_i)$. See Fig. 6 for the details.

Conversely, a spread of Doppler shifts is generally observed across the NLoS scatters, as widely described by the Jakes' scatter model [37], [65]. From an abstract point of view, so the ambiguity of reflectors is stochastically tailored into the wide-sense stationary uncorrelated scattering (WSSUS) modeling [66], [67]. The classical Jakes' fading model writes the Doppler power spectral density (PSD) as

$$S_{Jakes}(f;f_d)=\begin{cases}\dfrac{1}{\pi f_d\sqrt{1-\left(\frac{f}{f_d}\right)^2}} & |f|<f_d\\ 0 & \text{otherwise}\end{cases}, \qquad (3)$$

in the baseband domain. As a dual measure, the autocorrelation function (ASF) characterizes this fading model by $R_{\text{Jakes}}(\tau)=\int_{-\infty}^{\infty}S_{Jakes}(f;f_d)e^{j2\pi f\tau}df = J_0(2\pi f_d\tau)$ from Wiener-Khinchine Theorem, where $J_0(\cdot)$ denotes the first kind Bessel function of order 0. From these models, we derive the overall PSD of

$$S_{S_3}(f)=\sum_{i\in\Omega_L}\rho_i\delta(f-\alpha_i f_d)+S_{Jakes}(f;f_d)\left(\sum_{j\in\Omega_N}\rho_j+\sum_{\substack{j\neq k\\ j,k\in\Omega_N}}\sqrt{\rho_j\rho_k}\cos 2\pi f|\tau_j-\tau_k|\right). \qquad (4)$$

Fig. 7 shows the Doppler spectrum of this composite channel, S_3 *Mobile*. As is shown, three distinct peaks are observed above

[8] See Table XI in Appendix A for the GPS coordinates of transmission sites.

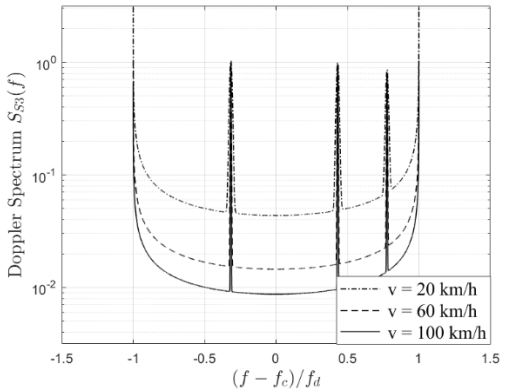

Fig. 7. Doppler spectrum $S_{S3}(f)$ of S_3 *Mobile* channel (Eq. (4), Dirac delta function approximated by $\delta(x) = 1/a/\sqrt{\pi}e\text{-}x^2/a^2$ for $a = 1/6$, $f_c = 700$ MHz).

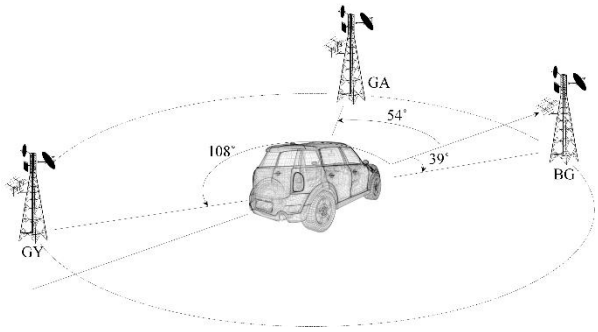

Fig. 8. Illustration of possible geometry that S_3 *Mobile* represents.

the curvature of noisy spectra.

Note that the description of S_3 *Mobile* is not restricted to a special topology example shown in Fig. 6. Although every LoS signal source in Fig. 6 is seen to be located south of $\mathbf{P}_{S3}$, the S_3 models are applicable to the *surrounded* reception scenarios as well. S_3 *Mobile* can represent urban receptions at the interior spots surrounded by SFN transmitters. Fig. 8 shows a possible geometry that includes three LoS components, in which a mobile receiver is surrounded by several transmitters but urbanity screens some of them to be NLoS sources.

D. Extension of S_3 and Stochastic Reformulation

1) S_3-Extended Model

Simple modeling has been widely sought in papers, such as [68] and [37], to ease the use of channel models for different test and planning tasks. The previous, S_3 *Fixed* and S_3 *Mobile* channels follow this principle, so minor energy contributions (to the impulse response) were neglected on purpose. These are NLoS paths tagged in Fig. 4 as #2-1, #4-1, and #6-1, whose indices imply that they originate in the same tower with main taps #2, #4, and #6, respectively. If those multipaths are considered not negligible, the channel model can alternatively be extended to include the visible secondary multipath peaks, as defined in Table VI.

Since those multipath taps are basically NLoS components, those are defined to share the same Doppler drift properties with other NLoS taps. In turn, the Doppler spectrum of this S_3-*Extended* model follows the analytical model in (4) if a mobile scenario is considered. To be clarified, this extension is not limited to the mobile model but also applied to the

stationary model S_3 *Fixed*. To this end, the phase shift values for the new multipath taps are determined in the same manner with S_3 *Fixed*, and are also used as the initial phase shift values in S_3 *Mobile-Extended*.

2) Stochastic Reformulation of Signal Envelope for Random Process Analysis

For certain research cases, the model can be reformulated into a stochastic variant to assist tractable analysis. One can consider the envelopes of NLoS components to be Rayleigh-distributed random variables, while keeping the direct path components deterministic. The normalized fading gain can be modeled as a combination of scalar constants (LoS elements) and complex Gaussian variables (Rayleigh elements), such as:

$$h(t) = \sum_{i\in\Omega_{\mathrm{L}}} \sqrt{\rho_i} e^{-j\theta_i} \delta(t-\tau_i) + \sum_{k\in\Omega_{\mathrm{N}}} g_k \delta(t-\tau_k), \quad (5)$$

where g_k is the channel gain of NLoS tap $\#k \in \Omega_N$. g_ks herein are given as zero-mean, i.i.d. complex Gaussian random variables, whose variance is $\rho_k > 0$ for each $k \in \Omega_{\mathrm{N}}$.

The dynamics in $h(t)$ relies solely on the randomness of g_ks, laying $2|\Omega_{\mathrm{N}}|$ of degree of freedom (DoF). Following this derivation, Table VI is considered the case that $|\Omega_{\mathrm{L}}| = 3$ and $|\Omega_{\mathrm{N}}| = 6$ hold and hence the DoF is given as $2|\Omega_{\mathrm{N}}| = 12$. Speaking shortly, the determinants for overall fading gain, dealt with as the primary statistic in wireless theory, are distributed over $2|\Omega_{\mathrm{N}}|$-DoF variables. If an ideal maximum ratio combining (MRC) is assumed, the receiver overall attains $\sum_{i\in\Omega_{\mathrm{L}}} \rho_i + \sum_{j\in\Omega_{\mathrm{N}}} \|g_j\|^2$ of fading gain, and thus the summation of NLoS part variables follows a generalized chi-square distribution. A probability density function (pdf) of the channel envelope then turns out to be

$$p(r) = \sum_{j\in\Omega_{\mathrm{N}}} \frac{e^{-\frac{r-\sum_{i\in\Omega_{\mathrm{L}}}\rho_i}{\rho_j}}}{\rho_j \prod_{\substack{j\neq k \\ j,k\in\Omega_{\mathrm{N}}}} \left(1-\frac{\rho_k}{\rho_j}\right)} u\left(r-\sum_{i\in\Omega_{\mathrm{L}}}\rho_i\right), \quad (6)$$

where $u(\cdot)$ denotes the unit step function [69].

Fig. 9(a) depicts the pdf and cumulative density function of this fading gain under S_3-*Extended* model. As can be inferred in the piecewise unimodal definition of (6), the fading gain is concentrated in the range of $[\sum_{i\in\Omega_{\mathrm{L}}}\rho_i, \infty)$ because LoS contributions are always present. Such tractable modeling is seen as a useful tool for building probabilistic insights on SFN, where it enables deriving outage probability and evaluating the quality of service on a network scale.

Remark. (Level crossing rate): In reality, the Doppler effect drives the receiver to experience time-varying fluctuations that might require attention, especially at the marginal field strength where the received signal-to-noise ratio (SNR) can drop below the requirement for successful decoding. Particularly for broadcast systems, channel coding and modulation lack instantaneous adaptivity, and hence such fluctuation behavior is of consideration.

The reformulation in (5) and (6) allows deriving a level crossing rate (LCR) to deal with such dynamics. LCR quantifies the channel behavior of how frequently the SNR crosses the threshold levels [69], thereby allowing analyses based on Markovian finite-state models.

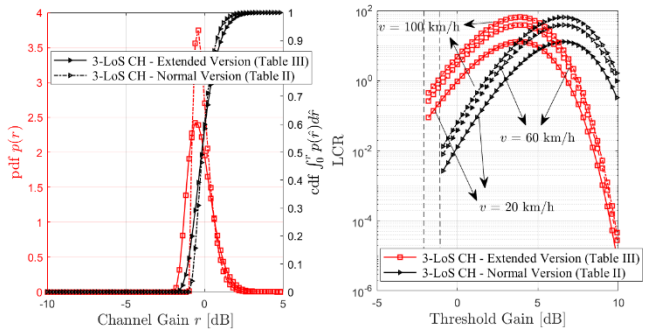

Fig. 9. (a: left) pdf and cumulative density function (cdf) of the chanel gain, (b: right) LCR vs. channel gain threshold (f_c = 700 [MHz]).

To analyze the dynamics of $h(t)$, the idea in [70] is applied for deriving the LCR of MRC-aggregated Rayleigh variables. By combining the results in [71] and [17] with (6), the LCR of the proposed model is derived as follows:

$$N_R(T) = \frac{f_d\sqrt{2\pi}}{\Gamma\left(\frac{\left(\sum_{\Omega_{\mathrm{N}}}\rho_j\right)^2}{\sum_{\Omega_{\mathrm{N}}}\rho_j^2}\right)} \left(\frac{\sum_{\Omega_{\mathrm{N}}}\rho_j}{\sum_{\Omega_{\mathrm{N}}}\rho_j^2}T\right)^{\frac{\left(\sum_{\Omega_{\mathrm{N}}}\rho_j\right)^2}{\sum_{\Omega_{\mathrm{N}}}\rho_j^2}-\frac{1}{2}} e^{-\frac{\sum_{\Omega_{\mathrm{N}}}\rho_j}{\sum_{\Omega_{\mathrm{N}}}\rho_j^2}T}, \quad (7)$$

for $T > \sum_{i\in\Omega_{\mathrm{L}}}\rho_i$. $\Gamma(z) = \int_0^\infty u^{z-1}e^{-u}\,du$ herein denotes the Gamma function for $\forall z > 0$. Note that $N_{\mathrm{R}}(T)$ is a unimodal function that has a unique maximum point. LCR of $h(t)$ is maximized at $T_{max} = \sum_{j\in\Omega_{\mathrm{N}}}\rho_j - \frac{\sum_{j\in\Omega_{\mathrm{N}}}\rho_j^2}{2\sum_{j\in\Omega_{\mathrm{N}}}\rho_j}$, achieving the global maximum $N_{\mathrm{R}}(T_{\max}) = \frac{f_d\sqrt{2\pi}}{\Gamma\left(\zeta+\frac{1}{2}\right)}\left(\frac{\zeta}{e}\right)^{\zeta}$ for $\zeta = \frac{\left(\sum_{j\in\Omega_{\mathrm{N}}}\rho_j\right)^2}{\sum_{j\in\Omega_{\mathrm{N}}}\rho_j^2} - \frac{1}{2}$. This unimodality is well-described in the numerical visualizations of Fig. 9(b). It is also shown that the LCR increases by f_d, which implies that user mobility incurs more frequent drops beneath the required SNR level, thereby resulting more frequent decoding failures at the marginal field strength reception values.

E. Channel Modeling: 2-LoS (S_2) and Single LoS (S_1) Cases

The number of LoS components will be scarce if the signals are detected in dense urban area. Complex surroundings would block most of the LoS incidences, and this shadowing effect would further be intensified in the urban core [72]-[76]. Additionally, if fixed reception antennas are used, the antenna directivity pattern also will reduce the number of LoS contributions. Measurement locations $\mathbf{P}_{S2}$ and $\mathbf{P}_{S1}$ stand on behalf of 2-LoS and single-LoS situations, respectively, which encourage investigating the SFN channels with less LoS links than S_3 situation.

Fig. 10 and 11 show the channel-sounding results measured at $\mathbf{P}_{S2}$ and $\mathbf{P}_{S1}$, respectively. Following the same methodology as with previous models, they are translated into S_2 and S_1 model profiles listed in Table VII. The definitions of S_2 and S_1 models follow the same fashion as previous S_3 models.

One difference of S_2 *Mobile* and S_1 *Mobile* models lies in the

TABLE VII. HPHT SFN CHANNEL MODEL PROFILE: S_2 AND S_1 CHANNELS

Tap Index	2-LoS Case (S_2)					Single-LoS Case (S_1)				
	Rel. Power [dB]	Rel. Delay [us]	Type	Phase Shift [rad] (Stationary)	Doppler Spectrum (Mobile)	Rel. Power [dB]	Rel. Delay [us]	Type	Phase Shift [rad] (Stationary)	Doppler Spectrum (Mobile)
1	-6.50	-49.189814815	Rayleigh	4.855121	Classical	-9.46	-14.612268519	Rayleigh	4.855121	Classical
2	-9.54	-33.564814815	LoS	3.956079	$-f_d$ shift	-7.34	-9.403935185	Rayleigh	3.419109	Classical
3	0.00	0.000000000	LoS	0.000000	$+f_d$ shift	0.00	0.000000000	LoS	0.000000	$0.7f_d$ shift
4	-9.59	3.327546296	Rayleigh	3.419109	Classical	-1.33	14.033564815	Rayleigh	5.864470	Classical
5	-15.84	31.684027778	Rayleigh	5.864470	Classical	-13.00	32.407407407	Rayleigh	2.215894	Classical
6						-16.54	35.300925926	Rayleigh	3.758058	Classical

way defining the Doppler shifts for LoS taps. As discussed above, *S_3 Mobile* pursues a realistic description by deriving the amount of pure Doppler shifts from the coordinates of site locations. Conversely, we better focus on the representative cases in designing *S_2 Mobile* and *S_1 Mobile* channels, since the reduced number of LoS elements simplifies the problem. In the case of *S_2 Mobile*, the amounts of Doppler shifts on tap #2 and #3 are determined as $-f_d$ and f_d, respectively, so as to consider the worst case of mobility effect. This kind of approach lines up with the 0 dB echo channel in [37] and has been widely applied to phase modulation fading simulators.

On the other hand, the main tap Doppler shift of *S_1 Mobile* is defined as $0.7f_d$ ($\simeq 1/\sqrt{2}f_d$), which is laid from a root mean square (rms) average of possible Doppler shifts. Given the user speed v and for the angle of arrival (AoA) ψ, a Euclidean norm expectation on $|v\cos\psi|$ over ψ gives $(\frac{1}{2\pi}\int_0^{2\pi} v^2\cos^2\psi\, d\psi)^{1/2} = 1/\sqrt{2}v$, which directly brings the average Doppler shift $\bar{f}_s = 1/\sqrt{2}f_d$. Unlike the S_3 case and also different with S_2 either, Doppler effect on the only direct path of *S_1 Mobile* is described as an expected value considering every possible movement direction of the *typical* user [77].

This approach coincides with the mobile Rician designs, e.g., RA channels, of the celebrated COST 259 project. Therein, a 45˚ angle has been chosen as a typical value of the road orientation against the direct path [78]. Similarly, but from a slightly different angle, PO channel of DVB standard has assigned an arithmetic average value $0.5f_d$ for the LoS component. Note that equation (4) is still applicable to *S_2 Mobile* and *S_1 Mobile* channels as well. It is available to adjust the equation by plugging the proper values into each attribute set (e.g., Ω_L, Ω_N, $\{\tau\}_{i\in\Omega_L,\Omega_N}$, $\{\theta\}_{i\in\Omega_L,\Omega_N}$). Likewise, the analytic formulations (5)-(7) are also compatible with S_2 and S_1 models.

Interestingly, experiments also showed that the power of reflected rays often appears comparable to the direct rays. Tap #1 of S_2 and tap #4 of S_1 are the manifest examples, which will impose substantial Doppler spread on mobile reception. Additionally, which agrees with the SFN's characteristics, the power-delay profiles in Table VII are not monotonic over the delay domain, and the impact of pre-ghosts is shown as tangible.

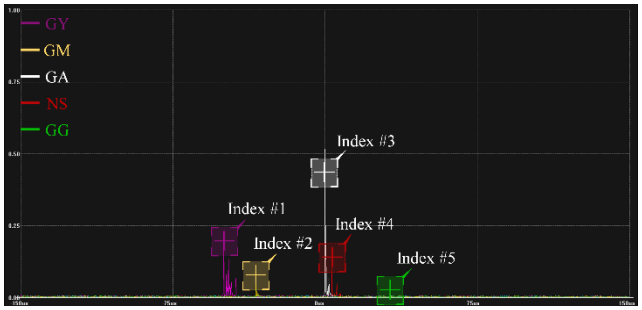

Fig. 10. SFN channel profile measured at $\mathbf{P}_{S2}$, Seoul Metropolitan (S_2 scenario, centered at 701 MHz, 6 MHz-width ATSC 3.0 DTV channel). The reflected rays from tower GY (tap #1) are found less attenuated than the direct path ray from tower GM (tap #2), due to the proximity.

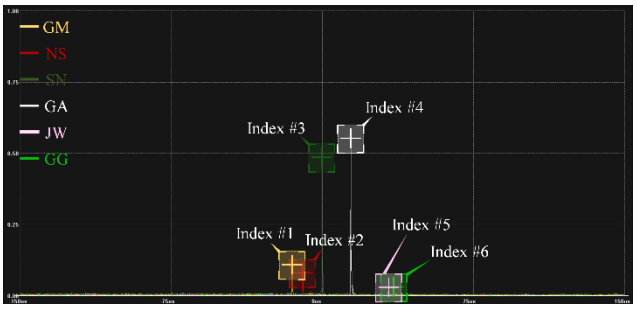

Fig. 11. SFN channel profile measured at $\mathbf{P}_{S1}$, Seoul Metropolitan (S_1 scenario, centered at 701 MHz, 6 MHz-width ATSC 3.0 DTV channel).

IV. CHANNEL MODELING IN LOW-POWER LOW-TOWER ENVIRONMENT: BASED ON THE DEPLOYMENT TOPOLOGY IN BENGALURU, INDIA

On the other hand, LPLT network deployment brings its own advantages in specific application cases. First, LPLT SFNs are compatible with short CP durations. Due to its gap-filling capability, portable and mobile reception also require LPLT network roll-outs if high coverage percentages are sought. An MBMS service in 3GPP networks is a classic example. As MBMS technology originates in cellular systems, MBSFNs are intimate with LPLT configurations. According to the European Telecommunication Standards Institute (ETSI) standard on Evolved Universal Terrestrial Radio Access (E-UTRA) [79], macrocell base stations can transmit up to 43 dBm (= 20 W) for downlink services over a 5 MHz bandwidth[9]. If 15 dBi antenna gain is considered, the ERP could reach 630 W but remains far

[9] Since we focus on the UHF band, reviewing Universal Mobile Telecommunications System (UMTS) might be helpful, whose macrocell transmit power ranges up to 36 dBm [80].

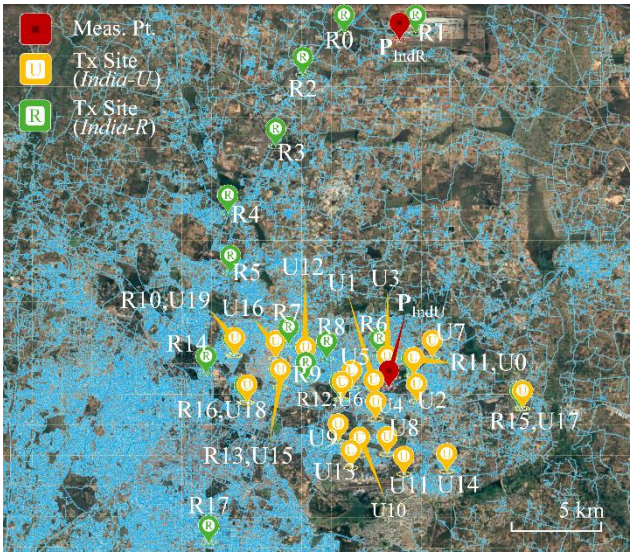

Fig. 12. Geographic topology of the Bengaluru SFN.

short of tens of kW. The height of such base stations lies in the typical range of 15 ~ 45 m, which lets the MBSFN be found as LPLT-based if it inherits this macrocell framework[10].

LPLT networks are also cost-efficient (or regulated to be constructed) in flat urban regions where building artificial high-towers might be difficult. Bengaluru in India is a good example in this context, particularly in contrast to the Seoul metropolitan area. Unlike the Seoul area, the Bengaluru plateau is overall flat across the territory, so it lacks an opportunity to establish a cost-efficient HPHT SFN in high-rise terrain. In this regard, the profiling for LPLT SFN here refers to the topography and network deployment status of the Bengaluru plateau.

The ingredients for modeling the proposed LPLT SFN channels, namely *India-U* and *India-R*, were obtained from a field propagation prediction tool *CRC-Predict* (*v. 3.21*) [81]. *India-U* and *India-R*, whose compositions are briefed in Table I, exemplify the urban and rural service areas in Bengaluru, respectively. Each LPLT's contribution was numerically simulated by computing the physical effects based on environmental data (e.g., terrain and clutter profiles). Most notably, the contributions of diffracted waves were computed on top of the Fresnel-Kirchhoff theory, relying on the canonical formula

$$E(x_{nxt}, z_{nxt}) = \sqrt{\frac{x_{prev}}{\lambda j\left(x_{nxt} - x_{prev}\right)}}$$

$$\int_{h_{prev}}^{\infty} E(x_{prev}, z_{prev}) e^{j\frac{2\pi}{\lambda}\sqrt{(x_{nxt}-x_{prev})^2+(z_{nxt}-z_{prev})^2}} dz_{prev}, \quad (8)$$

which describes the wave amplitude at (x_{nxt}, z_{nxt}). The computations were carried out in a segmented sense: $E(x_{\mathrm{nxt}}, z_{\mathrm{nxt}})$ was assumed to originate solely in the previous Huygens sources whose horizontal coordinate was x_{prev}. Herein, the variables indicated by scripts x and z denote the horizontal and vertical coordinates (altitudes), respectively; h_{prev} stands for the terrain or building elevation at x_{prev}; and λ denotes the wavelength $\lambda = c/f_c$.

For simulating the *India-U* and *India-R* profiles, the terrain and clutter data were segmented in 20 m intervals, i.e., $x_{\mathrm{nxt}} - x_{\mathrm{prev}} = 20$ m. The simulations used on-site infrastructure data from a commercial telecommunications network operator. Total 476 base stations were distributed over the 741 km^2 area of interest (AoI), leading to a station density of 0.6424 [sites/km^2]. Every base station counted in this profiling was considered to operate on the UHF radio channel 26 (CH 26, i.e., f_c = 514 MHz), and to radiate an ERP of 58.82 dBm through vertically polarized 3-sector antennas with 15 dBi gain.

The urban model *India-U* is based on the computations taken at $\mathbf{P}_{\mathrm{IndU}}$ (13˚00'07.48"N, 77˚40'68.32"E). At the same time, the model *India-R*, which exemplifies rural channels, is defined from the observations at $\mathbf{P}_{\mathrm{IndR}}$ (13˚11'31.78"N, 77˚41'19.05"E). According to the simulations, 20 towers' signals were accessible at the $\mathbf{P}_{\mathrm{IndU}}$, and the receiver at $\mathbf{P}_{\mathrm{IndR}}$ could detect signals from 18 different towers. Weak incidences were neglected if the wave strength did not reach 47 dBuV/m.

As presented in Fig. 12, those two observation points $\mathbf{P}_{\mathrm{IndU}}$ and $\mathbf{P}_{\mathrm{IndR}}$ faithfully express the environmental features for which they are respectively responsible. The rural site $\mathbf{P}_{\mathrm{IndR}}$ near the Bengaluru Airport received the signals from base stations with large ISD (reaches 5 km or 10 km); while the urban counterpart $\mathbf{P}_{\mathrm{IndU}}$, which was located in the central district, lied in a dense network area whose ISD ranged roughly from 1 km to 3 km.

Channel models listed in Table VIII and IX reflect those characteristics. We here point out that the plurality and denseness of CIR taps are the distinctive nature of urban LPLT SFN channels, as opposed to the HPHT counterpart. LPLT SFNs are denser due to the reduced cell coverage of each individual site. According to [34], at least tens of LPLTs are required to replace a single HPHT, and the requirement further increases when higher-powered HPHTs are considered. Which aligns with this context, the *India-U* profile in Table VIII shows rich echo effects and relatively short delay spread at the same time. Though it is said short, the 26.5 μs delay spread of *India-U* still overwhelms that of typical single-cell channel models because such a long delay spread is one of the identities of SFN.

Note that the strongest tap is labeled by index zero, namely as U0 and R0, and the others are sequentially tagged in the order of arrival time. The *India-U* model here shows pre-ghosts, which is another characteristic of SFN channels. On the other hand, *India-U* differs from the previous HPHT SFN models in terms of its LoS/NLoS distribution. *India-U* only consists of NLoS taps, whereas the Seoul SFN models include several direct path components. It is attributed to the insufficient elevation of LPLTs that usually brings continual shadowing in urban space [82]. In line with the measures applied to Seoul Metropolitan models, those NLoS taps' Doppler spreads are described by classical WSSUS Jakes' model.

On the contrary, *India-R* accompanies plural LoS taps, as shown in Table IX. The delay profile is found sparser than *India-U* as well. Precisely, four direct incidences are observed

[10] On another hand, 3GPP has lately endorsed new numerologies in its Rel-16 standard, such as 300 μs CP, so that it expands the ISD (up to 90 km) to enable HPHT operations.

in this rural case. The amounts of pure Doppler shifts at those LoS taps are derived from geographic data, similarly to the S_3 model. Again, multiple LoS taps are a unique identity of multi-source networks using a single frequency channel. Like the RA-class modeling in COST projects [37], *rurality* finds the channel more likely to have LoS connectivity. In SFN scenarios, such an increased LoS possibility is applied to multiple front-ends, resulting in the CIRs with plural LoS taps.

LPLT scenarios mostly exhibit the dominance of proximal transmitters. Accordingly, the LoS components of *India-R* are concentrated in the forepart, specifically the first four taps. The dominance of in-proxy transmitters' signals is seen in *India-R* channel and is demonstrated in *India-U* also. From the series of power-delay pairs listed in Table VIII, one can find that the CIR profile of *India-U* has a strong downtrend with respect to arrival delay – approximately to distance. For example, one can focus on the taps U0 ~ U14 by omitting the remaining part that includes exceptionally higher towers (≥ 75 m, see Table XI in Appendix A). The CIR envelope there follows an exponentially decreasing trend curve $P_{\text{rel}} = 1.5221e^{-1.258d}$, which guarantees the *R*-square statistics of $R^2 = 0.7809$. P_{rel} and d herein denote the relative power and tower distance, respectively.

Such dependence on transmitter proximity might let the urban-side LPLT SFN channels look similar to the conventional multipath models. Nevertheless, it shall be remembered that SFNs still possess the long delay spread property. The tail echoes presented in Table VIII reach tens of microseconds, whereas the single-cell multipath models have their echoes clustered within several microseconds.

The rural model *India-R* resembles multi-wave with diffuse power (MWDP) fading-class channels [83], [84], on the one hand. A significant amount of power is concentrated on the first four LoS taps, such that the sum power ratio is 7.68 dB between LoS and NLoS components[11]. Not only at the point of Doppler behavior, the difference between LoS and NLoS taps is but seen as distinctive in the power-delay profile also. There is a 21 dB gap of average power between the group {R0, ⋯, R4} and {R5, ⋯, R17}. Moreover, R5 is the first point where the standard deviation goes below 0.005, precisely 0.003942, when we sequentially remove the taps from the calculation set by starting from the first row of Table IX. That is, there is seen a homogeneity within each set {R0, ⋯, R4} and {R5, ⋯, R17} found along with the explicit contrast between them.

In case reduced complexity is required, weak taps can be neglected to downsize these LPLT SFN models. For example, if every tap whose relative power is beneath -20 dB is discarded, *India-U* and *India-R* channels are abstracted into a 10-tap channel and a 6-tap channel, respectively. Although such a simplification omits long-delay components, the delay spreads still dominate that of the single-cell scenarios. The maximum delay spread of reduced *India-U* remains at 26.5 μs while that of the *India-R* case turns out to be 62.6 μs, which is 35.3 μs shortened from the original 18-tap model. Recall that long lagging components tend to have weak response magnitude in these LPLT SFN models. Therefore, in case the model is to be simplified intentionally, the tap reduction threshold (i.e., cutoff magnitude) should be carefully determined to preserve SFNs' characteristics.

[11] In a similar fashion with the Rician *K*-factor.

TABLE VIII. LPLT SFN CHANNEL PROFILE: URBAN CASE IN BENGALURU (*INDIA-U*)

Station ID	Rel. Delay [us]	Type	Rel. Power [dB]	Phase Shift [rad] (Stationary)	Doppler Spectrum (Mobile)
U1	-2.1	NLoS	-1.9	4.8551	Classical
U2	-0.8	NLoS	-12.0	3.7580	Classical
U0	0.0	NLoS	0.0	0.0000	Classical
U3	0.5	NLoS	-6.4	3.4191	Classical
U4	1.3	NLoS	-12.5	5.4302	Classical
U5	1.9	NLoS	-21.7	0.1546	Classical
U6	4.1	NLoS	-11.5	2.2159	Classical
U7	4.6	NLoS	-9.7	5.8645	Classical
U8	8.2	NLoS	-22.2	3.0530	Classical
U9	9.4	NLoS	-24.6	0.6286	Classical
U10	9.9	NLoS	-17.2	1.0936	Classical
U11	11.9	NLoS	-28.5	3.4630	Classical
U12	11.9	NLoS	-29.1	3.6648	Classical
U13	12.0	NLoS	-29.4	2.8338	Classical
U14	14.8	NLoS	-30.6	3.3343	Classical
U15	16.6	NLoS	-21.7	5.9284	Classical
U16	18.3	NLoS	-27.4	1.0995	Classical
U17	21.2	NLoS	-14.7	3.9521	Classical
U18	23.5	NLoS	-24.9	2.1285	Classical
U19	26.5	NLoS	-19.8	5.7752	Classical

TABLE IX. LPLT SFN CHANNEL PROFILE: RURAL CASE IN BENGALURU (*INDIA-R*)

Station ID	Rel. Delay [us]	Type	Rel. Power [dB]	Phase Shift [rad] (Stationary)	Doppler Spectrum (Mobile)
R1	-6.8	LoS	-0.6	2.1388	$-0.7193f_d$ shift
R0	0.0	LoS	0.0	0.0000	$0.9528f_d$ shift
R2	9.6	LoS	-6.2	1.6336	$0.9371f_d$ shift
R3	21.8	LoS	-15.3	5.6888	$0.7615f_d$ shift
R4	37.7	NLoS	-28.0	4.8551	Classical
R5	46.4	NLoS	-27.6	3.7580	Classical
R6	52.6	NLoS	-26.6	3.4191	Classical
R7	53.8	NLoS	-28.5	5.4302	Classical
R8	54.2	NLoS	-27.9	0.1546	Classical
R9	59.6	NLoS	-27.2	2.2159	Classical
R10	60.3	NLoS	-18.7	5.8645	Classical
R11	60.7	NLoS	-23.1	3.0530	Classical
R12	61.9	NLoS	-27.7	0.6286	Classical
R13	62.6	NLoS	-19.2	1.0936	Classical
R14	66.6	NLoS	-24.5	3.4630	Classical
R15	66.8	NLoS	-22.9	3.6648	Classical
R16	67.4	NLoS	-26.6	2.8338	Classical
R17	97.9	NLoS	-28.0	3.3343	Classical

V. SUBURBAN MODEL FOR HETEROGENEOUS SFN USING BOTH HIGH AND LOW TOWERS: PROFILE FROM JEJU ISLAND SFN (J_2)

In practice, the network may instead be a heterogeneous mixture of HPHTs and LPLTs. Depending on the land use opportunities, some transmitters could be installed on hilly terrain, and some others could be deployed above high-rise

buildings, whereas the remainders should be located in low-rise residential areas.

The fading channel in this mixed SFN would be fabricated as a composite form, whose CIR profile has dense LPLT taps added at the foreside (early arrivals) part of the HPHT SFN's TDL model. Mixed SFNs partly resemble an urban/suburban example discussed in Section III: They are likely to have early arrivals from the shadowed sources and lagged arrivals of LoS signals. This kind of figure is attributed to (*a*) the proximity-dependent and prone-to-shadowing natures of urban-side LPLT SFNs; and simultaneously to (*b*) the HPHT SFN's characteristic likely to find open space incidences coming from far-distant sources.

This section focuses on portraying these aspects of mixed SFNs. To this end, a simple channel model J_2 is fabricated from the measurement data obtained in a suburban area of Jeju Island, South Korea [85] (see Table I). The experiments and channel modeling procedures followed the method described in Section III.

For field measurements, we constructed an ATSC 3.0 SFN distributing an experimental broadcasting service over Jeju Island. This experimental SFN consisted of three broadcast towers transmitting synchronized video signals. This physical network was viewed as a mixed SFN because those three participant towers were located on expressly different altitudes. Following the terminology in Fig. 14, the tower JDC was classified as a high-tower, whereas JVM and JYA were on moderate and low altitudes, respectively (see Table XII in Appendix A). Every tower emitted 4 kW ERP where the HPA output and antenna gain were 400 W and 10 dBi, respectively. As for the sounding reference signal, TxID signals were injected with -9.0 dB injection level. The measurements were taken using the test vehicle described in Section III-B, and every experiment was conducted on 689 MHz (CH 50).

The J_2 model includes two LoS taps. The channel profile in Table X specifies that the last two taps belong to LoS class, whereas the rest two are NLoS. Notably, the NLoS pre-ghost taps #1 and #2 precede the rest of the taps by 50 μs. Such a gap is well presented by green peaks in the measured CIR result Fig. 13.

As shown in Fig. 14, those incidences of tap #1 and #2 originated in the closest transmitter JYA but could not seize the direct visibility because the tower altitude was unduly low. The antenna elevation was about 30 m above the receive site $\mathbf{P}_{J2}$, and considerable terrain fluctuations appeared between JYA and $\mathbf{P}_{J2}$. J_2 is an example of a mixed SFN channel that realizes the early arrival of shadowed signals along with the delayed arrival of non-shadowed signals. Inheriting the worst-case-centric spirit underlying the design of S_2, the Doppler shifts are defined as $\pm f_d$ for the LoS taps #3 and #4, where the directions are given opposite to each other.

TABLE X. SFN CHANNEL MODEL PROFILE WITH MIXED TOWER CONFIGURATION: J_2 *FIXED* AND J_2 *MOBILE*

Tap Index	Rel. Power [dB]	Rel. Delay [us]	Type	Phase Shift [rad] (Stationary)	Doppler Spectrum (Mobile)
1	-5.11	-56.712962963	NLoS	4.855121	Classical
2	-5.66	-50.781250000	NLoS	3.419109	Classical
3	0.00	0.000000000	LoS	0.000000	$+f_d$ shift
4	-4.81	3.616898148	LoS	5.206899	$-f_d$ shift

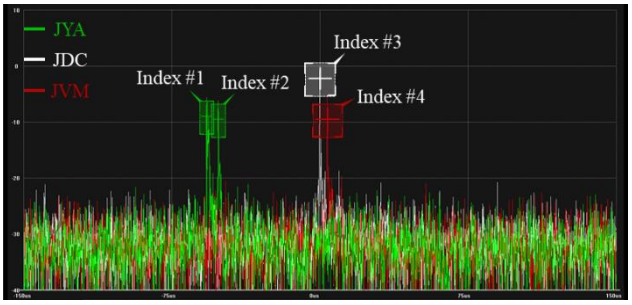

Fig. 13. SFN channel profile measured in Jeju SFN (centered at 689 MHz, 6 MHz-width ATSC 3.0 DTV channel).

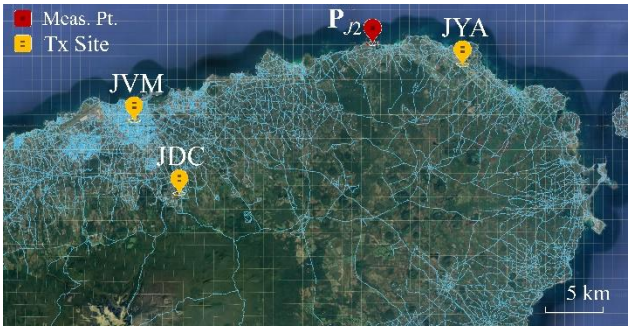

Fig. 14. SFN configuration in Jeju Island [85].

VI. DISCUSSIONS

This section discusses several topics related to some possibilities of SFN channels' future extension. We particularly discuss the effect of future repeater deployment, and model adaptation considering the antenna beam pattern. In addition, it is also discussed the effect of SFN operation in terms of service throughput.

A. *Effect of On-Channel Repeater Deployment*

After the initial deployment, generally, expanding the coverage (or filling up the voids therein) tends to rely more on repeaters than studio-connected transmitters. This repeater dependency is primarily due to the operation expenditure since the pure transmitters require dedicated STLs, which are costly to retain. This economic aspect urges SFNs to count the on-channel repeaters (OCRs) in the network.

The engagement of OCRs accompanies the increase of delay spread. The listen-and-retransmit mechanism of repeaters lengthens the overall propagation route by nature. In addition, the processing time of OCR machinery increases the latency even more. Another issue arises here: The processing delay poses a tradeoff against the quality of on-channel relay signals. Advanced OCRs [86] can cancel out the feedback interference and equalize the multipath-distorted input signal before retransmissions, instead consuming more time for those signal processing blocks. Otherwise, minor multipath distortions and even some portion of ISI will remain in the relay signals if such signal processing is not (or less) supported.

If advanced OCRs are used, the OCR-to-receiver channel

will be the only matter for distortion although the delay spread will increase. On the contrary, degraded functionalities of the equalization and feedback interference canceler will result in a sort of clustered taps (due to the ready-made distortions given to the OCR input) that pivot on each OCR-to-receiver propagation path; and would upraise the interference level. Instead, the delay spread will be less increased.

B. Modifications for Antenna Directivity

As mentioned in Section III-D, stationary reception use cases may accompany directional antennas. Likewise, some handheld devices could have adaptive antenna directivity as well. In this regard, one might attempt to tailor the SFN channel models again to emphasize the antenna directivity more.

If so, the contribution of the main tap should be highlighted (amplified) more, whereas off-the-main direction taps will be relatively suppressed at the same time. The simplest way is to give additional attenuations to the taps, precisely the amount gradually decreasing by the angular difference from the main tap's tower orientation. Every requisite geographic data is provided in this paper so that such treatments can be readily applied. A cutoff angle can be determined to omit the incidences whose angular difference is beyond the threshold, thereby reflecting the off-the-beam-neglecting nature. As well, realistic beam patterns could be applied to have sidelobes.

It is reasonable to consider an isotropic beam pattern for mobile receivers to use the proposed channel models without any modifications. Moreover, the nature of SFN, distributing the incidence opportunity across every orientation, encourages the feasibility of omnidirectional antennas in stationary scenarios. In fact, as discussed in Section III-D, the tap reduction in *S_2 Fixed* and *S_1 Fixed* models could already express the characteristics of stationary environments sufficiently.

C. Issues on Guard Interval (e.g., CP)

Long delay spread is one identity of SFNs, especially for HPHT SFNs. The results in Section III demonstrate that the long-lagging components can be even seen as comparably powerful to the main path signals. Therefore, if SFN is of interest, the OFDM transmissions shall guarantee a sufficient length of guard interval to avoid crucial ISI. So, despite its spectrum-economic identity, the SFNs might rather get rid of some throughput when viewed through a microscopic lens. This aspect brings another dimension of the coverage-throughput tradeoff to the scope. Nonetheless, it is widely verified that the rich signal superposition gain advantages SFNs to be found as explicitly beneficial.

VII. Conclusion

This paper introduced realistic fading channel models for terrestrial SFNs using the UHF band. The proposed models specifically characterized CIRs under three different classes of tower deployment: HPHT, LPLT, and mixed configurations. The HPHT SFN model was empirically designed by precise measurements drawn from an operating SFN in a metropolitan area. This work primarily focused on urban service areas, where the models addressed further subdivided cases according to receive-end conditions. In parallel, LPLT models were also formulated by means of physics-driven simulations based on on-site topology data. Similar to the HPHT case, mixed SFNs comprising both high and low towers were modeled from field data obtained in an experimental network's coverage. Throughout this paper, the unique identities of SFN transmission were discussed compared to the conventional single-cell channels. Using the TDL framework, we explored the effect of physical arrangement (e.g., urbanity, tower configuration, mobility, terrain profile, and others) on each channel attribute. As a result, this investigation contributes to the overall efficiency of SFN development. By improving the reference models to be more realistic, it is expected that the industry could accelerate the fine-tuning of SFN systems and related development processes.

TABLE XI. List of the Reference Point Locations – Seoul Metropolitan

Class	Site Indicator	GPS Coordinates
Tx	NS	37˚33'04.26"N, 126˚59'15.73"E
	GA	37˚26'25.25"N, 126˚57'51.08"E
	GG	37˚20'53.31"N, 127˚01'38.38"E
	GY	37˚33'11.99"N, 126˚42'51.00"E
	YM	37˚33'39.09"N, 127˚32'47.02"E
	BG	37˚37'45.05"N, 126˚54'31.65"E
	BN	37˚35'19.75"N, 126˚55'39.72"E
	JW	37˚36'39.60"N, 127˚02'36.69"E
	SN	37˚27'19.23"N, 127˚10'46.84"E
	GM	37˚28'15.92"N, 126˚51'40.16"E
Rx	$\mathbf{P}_{S3}$	37˚42'26.52"N, 126˚45'19.15"E
	$\mathbf{P}_{S2}$	37˚30'53.17"N, 126˚41'36.26"E
	$\mathbf{P}_{S1}$	37˚32'54.17"N, 127˚05'45.48"E

TABLE XII. List of the Reference Point Locations – Jeju Island

Class	Site Indicator	GPS Coordinates	Vertical Datum [m]	Building Height [m]
Tx	JDC	33˚27'03.37"N, 126˚34'18.96"E	357	16
	JVM	33˚30'06"N, 126˚31'45"E	65	25~30
	JYA	33˚32'33.28"N, 126˚48'44.14"E	25	10
Rx	$\mathbf{P}_{J2}$	33˚33'29.62"N, 126˚44'07.97"E	2	

Appendix A. GPS Coordinates of the SFN Transmitters and Measurement Points

This appendix provides the rationale data specifying the network entities' physical conditions. Table XI first presents the GPS coordinates of every tower included in the Seoul Metropolitan SFN. Note that the other detailed tower information is shown in Table III. Table XII and XIII list the information of Jeju and Bengaluru SFNs, respectively. Particularly for *India-U* and *India-R* models obtained from numerical simulations, the calculated results of absolute field strengths are enumerated in Table XIII, also identifying to which taps (towers) they belong. The location information herein is utilized for visualizing the topologies into Fig. 1, Fig. 12, and Fig. 14.

TABLE XIII. LIST OF THE REFERENCE POINT LOCATIONS – BENGALURU

Tap Index	*India-U*				Tap Ind.	*India-R*				Polarization / ERP
	Distance [km]	Field Strength [dBuV/m]	GPS Coordinates	Elevation [m]		Distance [km]	Field Strength [dBuV/m]	GPS Coordinates	Elevation [m]	
U1	1.1	76.1	12˚59'49.164"N, 77˚40'26.904"E	40	R1	1.4	82.5	77˚41'54.118"N, 13˚12'01.451"E	27	Vertical / 762.1843 W
U2	1.5	66	12˚59'24.432"N, 77˚41'15.900"E	26	R0	3.5	83.1	13˚12'05.544"N, 77˚39'28.152"E	16	
U0	1.7	78	13˚00'32.292"N, 77˚41'48.696"E	29	R2	6.3	76.9	13˚10'18.120"N, 77˚38'01.140"E	40	
U3	1.9	71.6	77˚40'26.904"N, 12˚59'49.164"E	26	R3	10	67.8	13˚07'58.368"N, 77˚37'06.672"E	14	
U4	2.1	65.5	12˚59'04.127"N, 77˚40'32.195"E	30	R4	14.8	55.1	13˚05'46.500"N, 77˚35'37.500"E	35	
U5	2.3	56.3	13˚00'06.947"N, 77˚39'41.543"E	24	R5	17.4	55.5	13˚03'58.716"N, 77˚35'32.964"E	32	
U6	3	66.5	12˚59'44.592"N, 77˚39'22.248"E	40	R6	19.3	56.5	13˚01'06.852"N, 77˚40'40.980"E	26	
U7	3.1	68.3	13˚01'05.771"N, 77˚42'20.411"E	29	R7	19.6	54.6	13˚01'33.239"N, 77˚37'33.239"E	34	
U8	4.2	55.8	12˚57'52.739"N, 77˚40'53.795"E	26	R8	19.7	55.2	13˚01'06.348"N, 77˚38'50.928"E	29	
U9	4.5	53.4	12˚58'19.991"N, 77˚39'14.471"E	28	R9	21.3	55.9	13˚00'23.471"N, 77˚38'07.619"E	28	
U10	4.7	60.8	12˚57'49.032"N, 77˚39'55.044"E	33	R10	21.5	64.4	13˚01'12.792"N, 77˚35'43.332"E	75	
U11	5.3	49.5	12˚57'19.583"N, 77˚41'28.643"E	40	R11	21.7	60	12˚59'49.164"N, 77˚40'26.904"E	40	
U12	5.3	48.9	13˚00'52.991"N, 77˚38'08.015"E	26	R12	22	55.4	12˚59'44.592"N, 77˚39'22.248"E	40	
U13	5.3	48.6	12˚57'32.255"N, 77˚39'40.463"E	26	R13	22.2	63.9	13˚00'08.748"N, 77˚37'15.456"E	84	
U14	6.1	47.4	12˚57'23.543"N, 77˚42'52.487"E	28	R14	23.4	58.6	13˚00'34.704"N, 77˚34'44.436"E	32	
U15	6.7	56.3	13˚00'08.747"N, 77˚37'15.455"E	84	R15	23.5	60.2	12˚59'25.512"N, 77˚45'21.024"E	100	
U16	7.2	50.6	13˚01'06.059"N, 77˚37'06.023"E	28	R16	23.7	56.5	12˚59'44.735"N, 77˚36'07.595"E	34	
U17	8.1	63.3	12˚59'25.511"N, 77˚45'21.023"E	100	R17	32.8	55.1	12˚54'55.224"N, 77˚34'48.936"E	100	
U18	8.8	53.1	12˚59'44.735"N, 77˚36'07.595"E	34						
U19	9.7	58.2	13˚01'12.792"N, 77˚35'43.332"E	75						
$\mathbf{P}_{INDU}$			13˚00'07.48"N, 77˚40'58.32"E		$\mathbf{P}_{INDR}$			13˚11'31.78"N, 77˚41'19.05"E		

REFERENCES

[1] *ATSC Standard: Physical Layer Protocol*, Washington, DC, USA, Doc. A/322:2021, Jan. 2021.

[2] ITU-R Report BT.2386-0, *Digital terrestrial broadcasting: Design and implementation of single frequency networks (SFN)*, Jul. 2015.

[3] J. Lee *et al.*, "Transmitter identification signal detection algorithm for ATSC 3.0 single frequency networks," *IEEE Trans. Broadcast*., vol. 66, no. 3, pp. 737-743, Sep. 2020.

[4] [Online] *Watch NextGenTV The Future of Television has Arrived*, WatchNextGenTV. Available: https://www.watchnextgentv.com/ (accessed on: Jun. 30, 2021).

[5] J. O'Neal, "Broadcast TV's future may lie in single frequency networks," *TVTechnology*, Mar. 2021. [Online] Available: https://www.tvtechnology.com/news/broadcast-tvs-future-may-lie-in-single-frequency-networks (accessed on: Oct. 28, 2021).

[6] *Authorizing Permissive Use of the "Next Generation" Broadcast Television Standard (FCC)*. [Online] Available: https://www.govinfo.gov/content/pkg/FR-2018-02-02/pdf/2018-01473 (accessed on: Oct. 28, 2021).

[7] P. Angueira *et al*., "DTV reception quality field tests for portable outdoor reception in a single frequency network," *IEEE Trans. Broadcast*., vol. 50, no. 1, pp. 42-48, Mar. 2004.

[8] G. Guerra *et al*., "Field measurement based characterization of the wideband urban multipath channel for portable DTV reception in single frequency networks," *IEEE Trans. Broadcast*., vol. 51, no. 2, pp. 171-179, Jun. 2005.

[9] L. Fay *et al*., "An overview of the ATSC 3.0 physical layer specification," *IEEE Trans. Broadcast*., vol. 62, no. 1, pp. 159-171, Mar. 2016.

[10] I. Eizmendi *et al*., "DVB-T2: The second generation of terrestrial digital video broadcasting system," *IEEE Trans. Broadcast.*, vol. 60, no. 2, pp. 258-271, Jun. 2014.

[11] J. A. Kutzner and D. Lung, "Predicting ATSC 3.0 broadcast coverage," *IEEE Trans. Broadcast*., vol. 62, no. 1, pp. 281-288, Mar. 2016.

[12] L. Wang *et al*., "Intelligent user-centric networks: Learning-based downlink CoMP region breathing," *IEEE Trans. Veh. Technol.*, vol. 69, no. 5, pp. 5583-5597, May 2020.

[13] M. Simon *et al*., "ATSC 3.0 broadcast 5G unicast heterogeneous network converged services starting Release 16," *IEEE Trans. Broadcast*., vol. 66, no. 2, pp. 449-458, Jun. 2020.

[14] D. Gómez-Barquero *et al*., "IEEE transactions on broadcasting special issue on: convergence of broadcast and broadband in the 5G Era," *IEEE Trans. Broadcast*., vol. 66, no. 2, pp. 383-389, Jun. 2020.

[15] J. Lee *et al*., "IP-based cooperative services using ATSC 3.0 broadcast and broadband," *IEEE Trans. Broadcast.*, vol. 66, no. 2, pp. 440-448, Jun. 2020.

[16] S. Ahn *et al*., "Mobile performance evaluation for ATSC 3.0 physical layer modulation and code combinations under TU-6 channel," *IEEE Trans. Broadcast*., vol. 66, no. 4, pp., Dec. 2020.

[17] S. Ahn *et al*., "Cooperation between LDM-based terrestrial broadcast and broadband unicast: On scalable video streaming applications," *IEEE Trans. Broadcast*., vol. 67, no. 1, pp. 2-22, Mar. 2021.

[18] Y. Wu *et al.*, "Cloud transmission: A new spectrum-reuse friendly digital terrestrial broadcasting transmission system," *IEEE Trans. Broadcast.*, vol. 58, no. 3, pp. 329-337, Sep. 2012.

[19] W. Li *et al.*, "Using LDM to achieve seamless local service insertion and local program coverage in SFN environment," *IEEE Trans. Broadcast.*, vol. 63, no. 1, pp. 250-259, Mar. 2017.

[20] J. J. Gimenez *et al*., "5G new radio for terrestrial broadcast: A forward-looking approach for NR-MBMS," *IEEE Trans. Broadcast.*, vol. 65, no. 2, pp. 356-368, Jun. 2019.

[21] 3GPP TR 36.819 V11.2.0, *3rd Generation Partnership Project; Technical Specification Group Radio Access Network; Coordinated Multi-Point Operation for LTE Physical Layer Aspects (Release 11)*, Sep. 2013.

[22] Y. Zhang *et al*., "MBSFN or SC-PTM: How to efficiently multicast/broadcast," *IEEE Trans. Broadcast.*, vol. 67, no. 3, pp. 582-592, Sep. 2021.

[23] Y. Zhang *et al*., "Mode selection algorithm for multicast service delivery," *IEEE Trans. Broadcast.*, vol. 67, no. 1, pp. 96-105, Mar. 2021.

[24] S. Ahn *et al*., "Large-scale network analysis on NOMA-aided broadcast/unicast joint transmission scenarios considering content popularity," *IEEE Trans. Broadcast*., vol. 66, no. 4, pp. 770-785, Dec. 2020.

[25] G. Araniti *et al.*, "Multicasting over emerging 5G networks: Challenges and perspectives," *IEEE Network*, vol. 31, no. 2, pp. 80-89, Mar./Apr. 2017.

[26] D. Mi *et al*., "Demonstrating immersive media delivery on 5G broadcast and multicast testing networks," *IEEE Trans. Broadcast*., vol. 66, no. 2, pp. 555-570, Jun. 2020.

[27] 3GPP TS 25.346 V7.6.0, *Introduction of the Multimedia Broadcast Multicast Service (MBMS) in the Radio Access Network (RAN); Stage 2 (Release 7)*, Dec. 2007.

[28] A. Sengupta *et al*., "Cellular terrestrial broadcast – Physical layer evolution from 3GPP Release 9 to Release 16," *IEEE Trans. Broadcast*., vol. 66, no. 2, pp. 459-470, Jun. 2020.

[29] S. Ahn *et al.*, "Converged distribution of 5G media: Opportunities of overlaid broadcast and emerging applications over dual connectivity," to be published in *IEEE Trans. Broadcast*.

[30] 3GPP TR 36.976 V1.0.0, "Overall description of LTE-based 5G broadcast (release 16)," Dec. 2019.

[31] ETSI TS 103.720 V1.1.1, "5G Broadcast System for linear TV and radio services; LTE-based 5G terrestrial broadcast system," Dec. 2020.

[32] 3GPP TS 36.213 V16.1.0, "Physical layer procedures (release 16)," Mar. 2020.

[33] C. Li *et al.*, "Planning Large Single Frequency Networks for DVB-T2," *IEEE Trans. Broadcast*., vol. 61, no. 3, pp. 376-387, Sep. 2015.

[34] U. Meabe *et al.*, "On the coverage and cost of HPHT versus LPLT networks for rooftop, portable, and mobile broadcast services delivery," *IEEE Trans. Broadcast*., vol. 61, no. 2, pp. 133-141, Jun. 2015.

[35] R. Irmer *et al*., "Coordinated multipoint: Concepts, performance, and field trial results," *IEEE Commun. Mag*., pp. 102-111, Feb. 2011.

[36] S. Ahn *et al*., "Fronthaul compression and precoding optimization for NOMA-based joint transmission of broadcast and unicast services in C-RAN," *IEEE Trans. Broadcast*., vol. 66, no. 4, pp. 786-799, Dec. 2020.

[37] ETSI TR 101.290 V1.4.1, *Digital Video Broadcasting (DVB), Measurement Guidelines for DVB Systems*, Jun. 2020.

[38] ETSI TR 102.377 V1.4.1, *Digital Video Broadcasting (DVB); DVB-H Implementation Guidelines*, Jun. 2006.

[39] ETSI EN 300.744 V1.6.2, *Digital Video Broadcasting (DVB); Framing structure, channel coding and modulation for digital terrestrial television*, Oct. 2015.

[40] Mackenzie, ABERT, and SET, "General description of laboratory tests," *DTV Field Test Report in Brazil*, Jul. 2000.

[41] ETSI TR 125.943 V15.0.0, *Universal Mobile Telecommunications System (UMTS); Deployment aspects*, Jul. 2018.

[42] COST207, "Digital land mobile radio communications," Final report, 1989.

[43] H. Parviainen *et al.*, "Novel radio channel models for evaluation of DVB-H broadcast systems," in *Proc. IEEE PIMRC*, Helsinki, Finland, Sep. 2006.

[44] ITU-R Rec. M.1225, *Guidelines for Evaluation of Radio Transmission Technologies for IMT-2000*, 1997.

[45] S. Jeon *et al*., "Field trial results for ATSC 3.0 TxID transmission and detection in single frequency network of Seoul," in *Proc. IEEE BMSB*, Valencia, Spain, Jun. 2018.

[46] J. Song, Z. Yang, and J. Wang, *Digital Terrestrial Television Broadcasting: Technology and System*, Piscataway, NJ, USA: Wiley, 2015.

[47] D. Plets *et al*., "On the methodology for calculating SFN gain in digital broadcast systems," *IEEE Trans. Broadcast*., vol. 56, no. 3, pp. 331-339, Sep. 2010.

[48] *ATSC Standard: Guidelines for the Physical Layer Protocol*, Washington, DC, USA, Doc. A/327:2021, Jan. 2021.

[49] S.-I. Park *et al.*, "ATSC 3.0 transmitter identification signals and applications," *IEEE Trans. Broadcast*., vol. 63, no. 1, pp. 240-249, Mar. 2017.

[50] S. Ahn *et al.*, "Probabilistic analysis on RF-watermark TxID detection in SFN with randomly distributed co-channel interferers and preamble cancellation," *IEEE Access*, vol. 8, pp. 56300-56311, Mar. 2020.

[51] S. Kwon *et al*., "Detection schemes for ATSC 3.0 transmitter identification in single frequency network," *IEEE Trans. Broadcast*., vol. 66, no. 2, pp. 229-240, Oct. 2019.

[52] A. V. Alejos, M. G. Sanchez, and L. Cuinas, "Improvement of wideband radio channel swept time-delay cross-correlation sounders by using Golay sequences," *IEEE Trans. Veh. Technol*., vol. 56, no. 1, pp. 362-368, Jan. 2007.

[53] G. L. Turin, "Introduction to spread-spectrum antimultipath techniques and their application to urban digital radio," *Proc. IEEE*, vol. 68, no. 3, pp. 328-353, Mar. 1980.

[54] N. E. Huang, Z. Shen, S. R. Long, "The empirical mode decomposition and the Hilbert spectrum for nonlinear and non-stationary – time series analysis," *Proc. R. Soc. Lond. A*, vol. 454, pp. 903–995, 1998.

[55] S.–I. Park *et al.*, "Performance analysis of all modulation and code combinations in ATSC 3.0 physical layer protocol," *IEEE Trans. Broadcast*., vol. 62, no. 2, pp. 197-210, Jun. 2019.

[56] J. Morgade *et al.*, "Coverage optimization for DVB-T/H single frequency networks using a PSO algorithm," in *Proc. IEEE BMSB*, Bilbao, Spain, Jun. 2009.

[57] *ATSC Standard: Scheduler / Studio to Transmitter Link*, Washington, DC, USA, Doc. A/324:2021, Mar. 2021.

[58] [Online] Available: https://earth.google.com (accessed on: Aug. 7, 2021).

[59] Korea Meteorological Administration, [Online] Available: https://weather.go.kr/ (accessed on: Aug. 28, 2021).

[60] P. Angueira *et al.*, "Fading caused by moving vehicles near the receiver on DTV (COFDM) 8-MHz signals," *IEEE Commun. Lett.*, vol. 6, no. 6, pp. 250-252, Jun. 2002.

[61] S. Ahn *et al*., "Multi-antenna diversity gain in terrestrial broadcasting receivers on vehicles: A coverage probability perspective," *ETRI Journal*, vol. 43, no. 3, pp. 400-413, Jun. 2021.

[62] U. Madhow, *Fundamentals of Digital Communication*, NJ, USA: Cambridge University Press, 2008.

[63] S. Haykin and M. Moher, *Modern Wireless Communications*, NJ, USA: Pearson Prentice Hall, 2005.

[64] A. Goldsmith, *Wireless Communications*, NJ, USA: Cambridge University Press, 2005.

[65] W. C. Jakes and C. D. Cox, *Microwave Mobile Communications*, Hoboken, NJ, USA: Wiley, 1994.

[66] P. A. Bello, "Characterization of randomly time-variant linear channels," *IEEE Trans. Commun. Syst.*, pp. 360-393, Dec. 1963.

[67] M. F. Pop and N. C. Beaulieu, "Limitations of sum-of-sinusoids fading channel simulators," *IEEE Trans. Commun*., vol. 49, no. 4, pp. 699-708, Apr. 2001.

[68] ETSI TR 101.190 V.1.3.2 *Digital Video Broadcasting (DVB), Implementation Guidelines for DVB Terrestrial Services, Transmission Aspects*, May, 2011.

[69] D. Hammarwall, M. Bengtsson, and B. Ottersten, "Acquiring partial CSI for spatially selective transmission by instantaneous channel norm feedback," *IEEE Trans. Sig. Process*., vol. 56, no. 3, pp. 1188-, Mar. 2008.

[70] X. Dong and N. C. Beaulieu, "Average level crossing rate and average fade duration of selection diversity," *IEEE Commun. Lett*., vol. 5, no. 10, pp. 396–398, Oct. 2001.

[71] M. F. Hanif and P. J. Smith, "Level crossing rates of interference in cognitive radio networks," *IEEE Trans. Wireless Commun*., vol. 9, no. 4, pp. 1283–1287, Apr. 2010.

[72] J. Brueckner, "The structure of urban equilibria: A unified treatment of the Muth-Mills model," *Handbook of Regional and Urban Economics: Urban Economics Vol. 2*, Amsterdam: North Holland Press, 1987.
[73] I. Atzeni, J. Arnau, and M. Kountouris, "Downlink cellular network analysis with LOS/NLOS propagation and elevated base stations," *IEEE Trans. Wireless Commun*., vol. 17, no. 1, pp. 142–156, Jan. 2018.
[74] S. Ahn *et al*., "Velocity optimization for UAV-mounted transmitter in linearly-varying population fields," under preparation.
[75] A. Al-Hourani, S. Kandeepan, and A. Jamalipour, "Modeling air-to-ground path loss for low altitude platforms in urban environments," in *Proc. IEEE GLOBECOM*, Austin, TX, USA, Dec. 2014.
[76] *Propagation Data and Prediction Methods Required for Design of Terrestrial Broadband Millimetric Radio Access System Operating in a Frequency Range About 20-50 GHz*, document Rec. ITU-R P.1410-2, 2005.
[77] M. Haenggi, *Stochastic Geometry for Wireless Networks*, New York, NY, USA: Cambridge Univ. Press, 2012.
[78] H. Asplund *et al*., "The COST 259 directional channel model – Part II: Macrocells," *IEEE Trans. Wireless Commun*., 5, no. 12, pp. 3434-3450, Dec. 2006.
[79] ETSI TR 136.942 V14.0.0, *LTE; Evolved Universal Terrestrial Radio Access (E-UTRA); Radio Frequency (RF) system scenarios*, Apr. 2017.
[80] ETSI TR 125.942 V15.0.0, *Universal Mobile Telecommunications System (UMTS); Radio Frequency (RF) system scenarios*, Jul. 2018.
[81] J. H. Whitteker, "Physical optics and field-strength predictions for wireless systems," *IEEE J. Sel. Areas Commun.*, vol. 20, no. 3, pp. 515-522, Apr. 2002.
[82] ETSI TR 138.901 V14.3.0, 5G; *Study on Channel Model for Frequencies from 0.5 to 100 GHz*, Jan. 2018.
[83] G. D. Durgin, T. S. Rappaport, and D. A. de Wolf, "New analytical models and probability density functions for fading in wireless communications," *IEEE Trans. Commun*., vol. 50, no. 6, pp. 1005-1015, Jun. 2002.
[84] Y. J. Chun, "A generalized fading model with multiple specular components," *arXiv preprint arXiv:1810.05258v1*, Oct. 2018.
[85] B. Lim *et al.*, "ATSC 3.0 field trial under 3-Tx SFN environments," in *Proc. IEEE BMSB*, Paris, France, Oct. 2020.
[86] S. Ahn *et al*., "Implementation and test results of on-channel repeater for ATSC 3.0 systems," to be published in *ETRI Journal*.
[87] S. Ahn *et al*., "Empirical modeling of UHF wireless channel in HPHT metropolitan SFNs," under preparation for *Proc. IEEE BMSB*, Bilbao, Spain, Jun. 2022.